



Interfacial hydrogen bonding-involved electrocatalytic ammonia synthesis on OH-terminated MXene

Jinmeng Cai^a, Jingjing Huang^a, Ang Cao^{b,*}, Yingying Wei^a, Huimin Wang^a, Xue Li^a, Zheng Jiang^c, Geoffrey I.N. Waterhouse^d, Siyu Lu^{a,*}, Shuang-Quan Zang^{a,*}

^a Green Catalysis Center, College of Chemistry, Zhengzhou University, Zhengzhou 450001, China

^b Department of Physics, Technical University of Denmark, Kongens Lyngby 2800, Denmark

^c Shanghai Synchrotron Radiation Facility, Shanghai Institute of Applied Physics, Chinese Academy of Sciences, Shanghai 201800, China

^d School of Chemical Sciences, The University of Auckland, Auckland 1142, New Zealand

ARTICLE INFO

Keywords:

Ti₃C₂ MXene

Terminal groups

Hydrogen bonding

Electrocatalytic nitrate reduction

Ammonia synthesis

ABSTRACT

MXene basal planes are generally considered catalytically inert, due to the passivation by inactive surface groups. However, theoretical calculation predicates that MXene basal planes can become active by tuning its terminal groups. The above understandings are ambiguous on whether the MXene basal planes are indeed electrocatalytically active, and in turn what are the true active sites on MXene. Herein, we functionalized Ti₃C₂ MXene by introducing terminal oxygen groups to reveal the active sites and probe the reaction mechanism for electrocatalytic nitrate reduction reaction (eNO₃RR). On the basis of the data presented, the in situ transformed surface hydroxyl groups were identified as a new active site for nitrate reduction. A novel reaction mechanism involving hydrogen-bonding (H-bonding) between nitrate and the -OH groups on the Ti₃C₂ MXene basal plane was proposed, which adequately explained the high applied potentials and low selectivity for HER on the OH-terminated Ti₃C₂ MXene during eNO₃RR. This hydrogen-bonding-mediated process is likely applicable to a wide range of other materials and reactions.

1. Introduction

Ammonia (NH₃) as an invaluable commodity chemical, is widely spreadly used in the manufacture of artificial fertilizers and other nitrogen-containing chemicals [1–4]. Electrochemical reduction of nitrate to ammonia (eNO₃RR) has recently been recognized as a viable alternative to the conventional Haber-Bosch process [5]. The reduction process only requires an ambient operating condition and can well utilize renewable electricity as energy source [6]. Generally, the nitrate reduction to ammonia involves eight-electron and nine-proton transfer processes ($\text{NO}_3^- + 9\text{H}^+ + 8\text{e}^- \rightarrow \text{NH}_3 + 3\text{H}_2\text{O}$) [7], and such complex pathways leads to the generation of many by-products such as N₂, NO and NO₂, which increases the difficulty of analyzing the mechanism. Furthermore, the competitive hydrogen evolution reaction (HER) and the ambiguous active sites under reaction condition are additional obstacles in the development of highly efficient electrocatalyst [8].

MXenes, an umbrella term for a family of two-dimensional (2D) transition metal carbides or nitrides, have been extensively studied in recent years for electrocatalysis due to their unique properties [9–11].

Theoretical investigations have predicted that MXenes are efficient electrocatalysts for NH₃ synthesis under ambient conditions, especially with exposed metal atoms [12,13]. Wang et al. reported that the edge planes with exposed Ti sites are preferred for the improved selectivity of NH₃, showing the potential of minimizing the size of MXene nanosheets for higher performance [14]. In above cases, MXene basal planes are generally considered catalytically inert, due to the passivation by inactive functional groups that prevents the adsorption of eNO₃RR reaction intermediates (Fig. 1a) [15]. However, a number of recent research works have reported that MXene basal planes can turn to be active in electrocatalytic reaction by tuning its terminal groups, especially with oxygen-functionalized surface [16,17]. Seh et al. reported the O-terminated W₂CO₂ and Ti₂CO₂ are promising CO₂ reduction reaction (CO₂RR) catalysts with low limiting potentials and good selectivity against the HER [18]. Singh et al. reported the group IV (Ti₂X and Zr₂X; X = C, N or B) MXenes with O-termination are favor the *HCOOH reaction pathway, lowering the potential toward efficient electrocatalytic CO₂RR [19]. These works raise paradoxical questions about whether the basal planes of MXenes are indeed electrocatalytically active, and in turn what are

* Corresponding authors.

E-mail addresses: angc@dtu.dk (A. Cao), sylu2013@zzu.edu.cn (S. Lu), zangsqzg@zzu.edu.cn (S.-Q. Zang).

<https://doi.org/10.1016/j.apcatb.2023.122473>

Received 1 December 2022; Received in revised form 25 January 2023; Accepted 14 February 2023

Available online 15 February 2023

0926-3373/© 2023 Elsevier B.V. All rights reserved.

the true active sites on MXenes. Resolving this issue will facilitate the rational design of MXene-based electrocatalysts with high activity and selectivity for NH_3 synthesis through eNO_3RR .

Currently, the influence of nonchemical bonding interactions (such as hydrogen bonds) on reaction pathways and catalytic processes is attracting the attention of researchers [20,21], which may be used to explain where the active sites are on the surface of MXenes protected by inactive functional groups. The Yang Shao-Horn research group revealed that the hydrogen bond interaction between ionic liquids and oxygen-reduction reaction (ORR) intermediates leads to significantly enhanced ORR activity [20]. The enhanced activity of ORR comes from the faster proton tunneling dynamics, thus generating greater ORR exchange current density. Wang's team proved that hydrogen bonds on the catalyst surface and in the bulk solution can inhibit oxidation and reverse reaction in photocatalytic dehydrocoupling of ethanol over Au/CdS, showing that nonchemical bonding interactions can steer the reaction paths of radicals for selective photocatalysis [21]. The findings highlight opportunities by tuning hydrogen-bond structures to control catalytic activity.

In this work, we functionalized the basal plane of a Ti_3C_2 MXene by introducing terminal oxygen groups to reveal the active sites and probe the reaction mechanism for eNO_3RR . The surface states of the Ti_3C_2 MXene catalyst before, during and after eNO_3RR was carefully characterized and the free energy diagrams of $\text{NO}_3^- \rightarrow \text{NH}_3$ process associated with different basal plane terminations was calculated. Combining the surface analysis and calculation, we identified for the first time that surface hydroxyls on the Ti_3C_2 MXene basal plane play a key role in the

stepwise reduction-hydrogenation of nitrate, whilst also inhibiting H_2 evolution. On the basis of the data presented, surface hydroxyl groups are identified as a new active site for nitrate reduction. A novel reaction mechanism involving hydrogen-bonding (H-bonding) between nitrate and the -OH groups on the Ti_3C_2 MXene basal plane was proposed (Fig. 1b), which adequately explained the high applied potentials and low selectivity for HER on the OH-terminated Ti_3C_2 MXene. This approach is likely applicable to a wide range of other materials and processes, highlighting new opportunities to enhance electrocatalytic performance through H-bonding interactions between adsorbates and electrocatalysts.

2. Experimental section

2.1. Chemicals

All chemical reagents were purchased (Shanghai Aladdin Bio-Chem Technology Co., LTD). No additional purification steps are required before use. Both K^{15}NO_3 and $(^{15}\text{NH}_4)_2\text{SO}_4$ are of high purity (99 atom% ^{15}N , purity > 98.5 %) for the isotope-labeling experiments.

2.2. Preparation of oxygen-functionalized MXene electrocatalyst

A $\text{Ti}_3\text{C}_2\text{T}_x$ MXene dispersion was prepared by etching and ultrasonic methods. Briefly, Ti_3AlC_2 powder (1 g) was added to an etching solution containing 1 g of LiF dissolved in 20 mL of 6 M HCl. The resulting dispersion was then heated at 35 °C under magnetic stirring for 24 h.

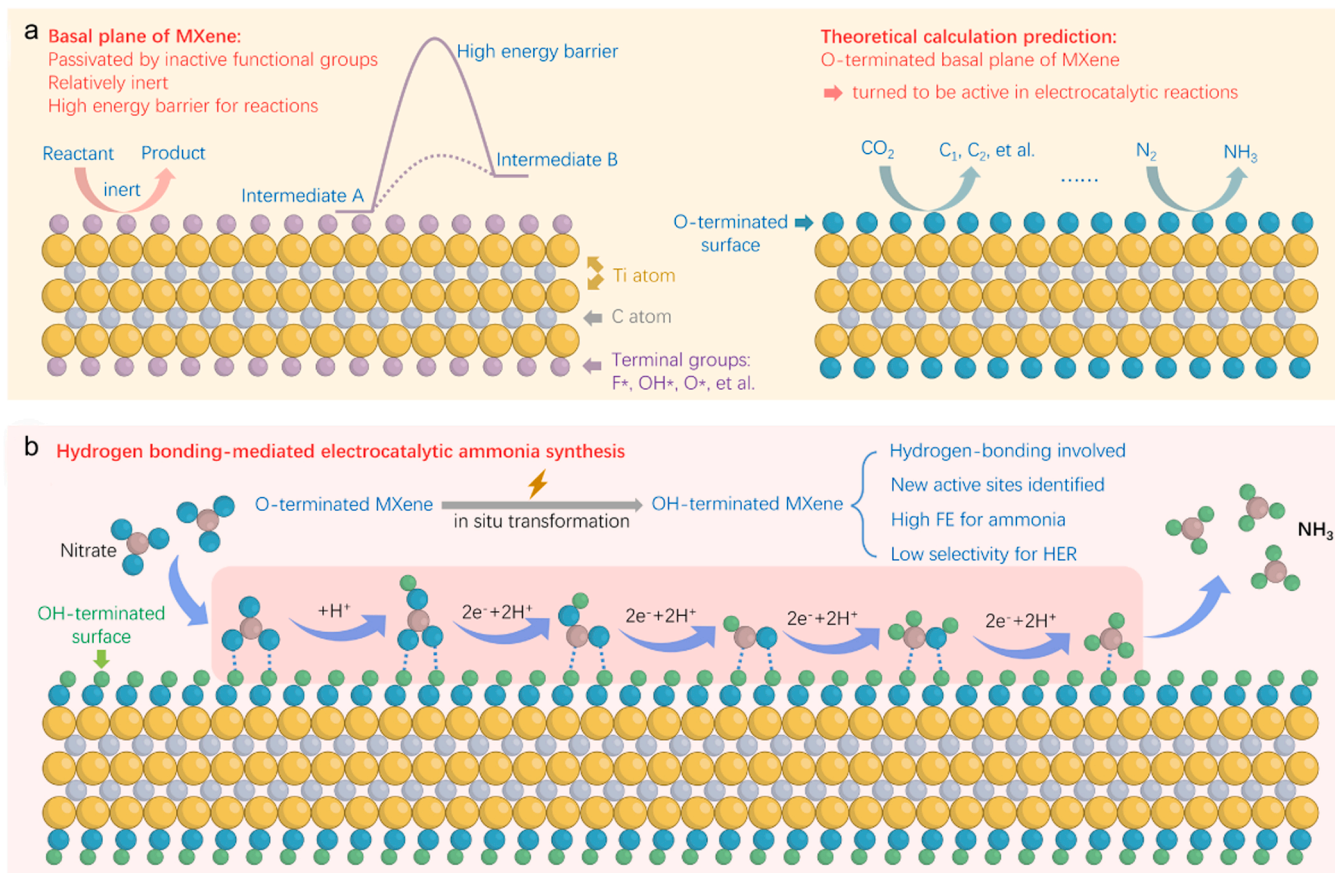


Fig. 1. Schematic comparison of properties and active sites on MXene basal planes with different terminal groups. (a) The passivation by inactive functional groups makes the MXene basal planes catalytically inert. However, theoretical calculation predicates that MXene basal planes can become active in electrocatalytic reactions by tuning its terminal groups to oxygen. (b) The O-terminated MXene can be converted to OH-terminated MXene in eNO_3RR process. The in situ transformed surface hydroxyl groups were identified as a new active site for eNO_3RR . A novel reaction mechanism involving hydrogen-bonding between nitrate and the -OH groups on the Ti_3C_2 MXene basal plane was proposed.

After the etching of the aluminum layers, the $\text{Ti}_3\text{C}_2\text{T}_x$ product was collected by centrifugation and washed repeatedly with deionized water until the washings were neutral. The solid was then dispersed in DI water by sonication for 1 h. The resulting aqueous $\text{Ti}_3\text{C}_2\text{T}_x$ MXene dispersion ($\text{Ti}_3\text{C}_2\text{T}_x$ MXene concentration $\sim 10 \text{ mg mL}^{-1}$) was stored in a refrigerator at 4°C under a N_2 atmosphere before use.

To prepare the working electrode, 50 μL of Nafion was added into 1 mL of the $\text{Ti}_3\text{C}_2\text{T}_x$ MXene dispersion to form a catalyst ink. After ultrasonication, 50 μL of the catalyst ink was dropped onto carbon paper ($1 \times 1 \text{ cm}^2$). After natural drying of the ink, the carbon paper was placed in a tube furnace and heated in an argon atmosphere containing trace amounts of oxygen at 400°C for 2 h. After cooling to room temperature, the oxygen-functionalized Ti_3C_2 MXene working electrodes were obtained.

2.3. Electrochemical nitrate reduction reaction

Electrochemical reactions were measured on an electrochemical workstation (CHI 660E, Chenhua, Shanghai). A typical H-type cell was used for the measurement. 0.5 M K_2SO_4 solution was used as the electrolyte in both cathode and anode compartment. Before the reaction, 200 ppm KNO_3 (NO_3^-/N) was added into the cathode compartment. The geometric surface area of the working electrode was used for the normalization of current density. The scanning rate of linear sweep voltammetry (LSV) was set as 10 mV s^{-1} . All curves were measured for continuous cycles until steady. For calculation of the Faradaic efficiency and selectivity, potentiostatic tests were performed at different applied potentials for 1 h.

2.4. Ion concentration detection

Ion chromatography (IC) was used to measure the concentrations of NH_4^+ , NO_2^- , and NO_3^- . Anions and cations require different chromatographic columns. For qualitative and quantitative measurements, standard curves for NH_4^+ , NO_2^- , and NO_3^- were prepared. Typically, NH_4^+ , NO_2^- , and NO_3^- solutions with different N concentrations in 0.5 M K_2SO_4 were prepared and their IC spectra collected. By plotting peak areas vs. ion concentrations, linear calibration plots were obtained for NO_2^- and NO_3^- . Due to the incomplete ionization of NH_4^+ in solution, a polynomial fitting was more appropriate to describe the IC response with NH_4^+ concentration. For the post-reaction electrolyte analyses, 250 μL of the used electrolyte was diluted to 5 mL and analyzed by IC. Based on the measured peak areas and standard curves, the concentrations of each ion in the sample were calculated.

2.5. Density functional theory (DFT) calculation method

A (4×4) supercell of the O-functionalized MXene monolayers was built as the calculation model and a vacuum region of 15 \AA was adopted to separate periodic vertical images. The optimized structures of the bulk phase and $\text{Ti}_3\text{C}_2\text{O}_2$ surfaces are shown in Figs. S24–25. The bottom two layers were fixed at their equilibrium bulk positions, whereas the rest of the layers and the adsorbates were allowed to relax during the geometric optimization until the forces on each atom were less than 0.05 eV/\AA .

The adsorption energy (ΔE) of adsorbed species on the model surface was calculated by

$$\Delta E(\text{species}) = E(\text{slab} + \text{H}_x\text{O}_y\text{N}_z) - E(\text{slab}) - xE_{\text{H}} - yE_{\text{O}} - zE_{\text{N}} \quad (1)$$

where $E(\text{slab})$ and $E(\text{slab} + \text{H}_x\text{O}_y\text{N}_z)$ mean the electronic energy of pristine Ti_3C_2 MXene without any functional group and species adsorbed on this surface, respectively. $E_{\text{H}} = 0.5E_{\text{H}_2}$, $E_{\text{O}} = E_{\text{H}_2\text{O}} - E_{\text{H}_2}$, and $E_{\text{N}} = E_{\text{HNO}_3} - 3E_{\text{H}_2\text{O}} - 2.5E_{\text{H}_2}$ are relative to the respective gas-phase energies, and x , y , and z are chosen to represent the number of hydrogen, oxygen, and nitrogen atoms in the adsorbed intermediate. We employ

the adsorption of HNO_3^* as a reference in drawing the free energy diagram.

The free energy (ΔG) is given by

$$\Delta G = \Delta E + \Delta E_{\text{ZPE}} + \int_0^T C_p dT - T\Delta S \quad (2)$$

where E_{ZPE} is the zero-point energy correction, C_p is heat capacity, ΔS is the entropy change, T is the absolute temperature (298.15 K). The limiting potential was calculated by taking the negative of the maximum free energy difference between each two successive steps in the free energy diagram.

The free energy change for adsorption of O_mH_n^* intermediates was computed as

$$\Delta G(\text{U, pH}) = G(\text{slab}) + mG_{\text{H}_2\text{O}} + G_{\text{slab, O}_m\text{H}_n^*} - (2m-n)(0.5G_{\text{H}_2} - U_{\text{SHE}} - 2.323k_B T \text{pH}) \quad (3)$$

$$U_{\text{SCE}} = U_{\text{SHE}} - 0.24 \quad (4)$$

where slab means the O-functionalized Of-TiMX surface with removing all oxygen atoms at the top layer. U_{SHE} is the potential relative to the standard hydrogen electrode (SHE). Therefore, we could derive a surface Pourbaix diagrams as a function of potential/pH for various adsorbates on the surface in reference to standard conditions when $\Delta G(\text{U, pH}) = 0$.

3. Results and discussion

3.1. Characterization of the oxygen-functionalized Ti_3C_2 MXene

The strategy for synthesizing the Ti_3C_2 MXene involved etching the Al layers from Ti_3AlC_2 powder using a mixed LiF-HCl solution to weaken the interlayer interactions (Fig. 2a). Next, the multi-layered Ti_3C_2 MXene (Fig. S1b) was ultrasonically exfoliated in ultrapure water to obtain single or few-layered Ti_3C_2 MXene (TiMX) [22,23]. A mild calcination treatment was then performed to convert TiMX to oxygen-functionalized TiMX (Of-TiMX). The stepwise conversion of Ti_3AlC_2 to TiMX and Of-TiMX was tracked by X-ray diffraction (XRD) (Fig. S2). The (104) peak centered at 39.1° of Ti_3AlC_2 disappeared with the concomitant emergence of a (002) peak centered at 7.2° associated with TiMX, demonstrating the successful etching and exfoliation [24]. The TiMX sample existed as very thin sheets with smooth and wrinkled surfaces by scanning electron microscopy (SEM) (Fig. 2b). Atomic force microscopy (AFM) revealed the average thickness of the nanosheets to be around 3.8 nm (Fig. 2c), or 2–3 MXene layers. Top-view transmission electron microscopy (TEM) images further confirmed that the exfoliated TiMX nanosheets contained only a few layers (Fig. 2d and Fig. S3). The surface morphology of Of-TiMX (Fig. 2e) was very similar to TiMX, comprising ultrathin nanosheets of a few layers (without sintering).

In order to further probe the surface structure of the two catalysts, we performed the high-resolution TEM (HRTEM) imaging and fast Fourier transform (FFT) pattern analyses. Fig. 2f reveals that TiMX possessed a highly crystalline lattice, with the FFT image (inset) showing a lattice of neatly arranged dots. Results indicate that TiMX contained few basal plane defects. After the oxygen-functionalization treatment, the HRTEM image and FFT image of Of-TiMX displayed slightly more disorder (Fig. 2i), which was expected due to the surface-functionalization by oxygen atoms [25]. We used inverse FFT (IFFT) to further investigate the structure changes that occurred after surface oxygen modification. After Fourier transform filtering (Fig. S4) to remove any interference information, IFFT images were obtained for TiMX and Of-TiMX (Fig. 2g, j). The similar lattice arrays of the two catalysts indicate that the oxygen-functionalization treatment did not destroy the intrinsic crystalline structure of the MXene. Small differences were found in lattice spacings for TiMX and Of-TiMX, with Of-TiMX having slightly smaller lattice spacings (Fig. 2h, k). This provides further evidence for the

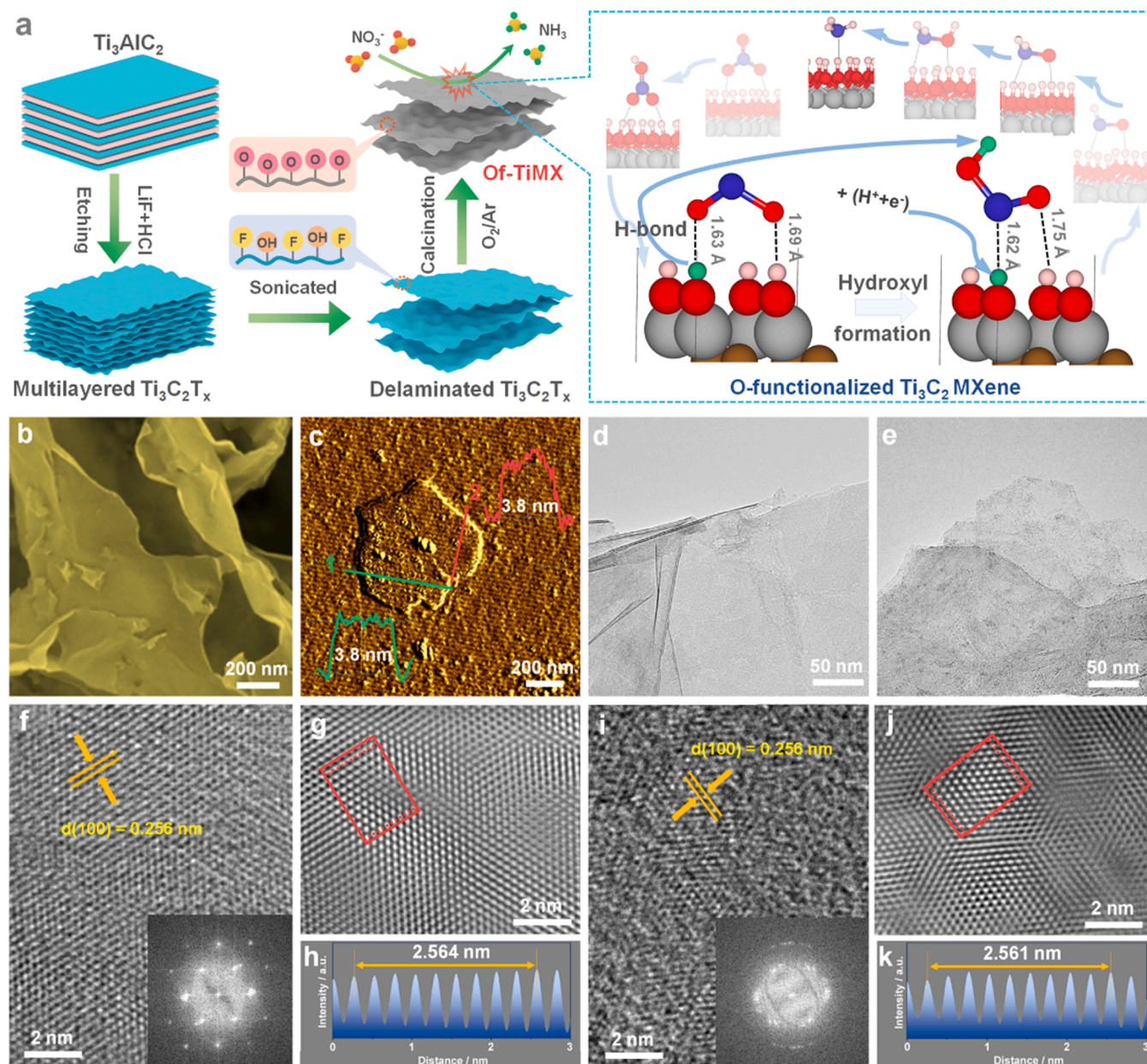


Fig. 2. Physical Characterizations of Ti₃C₂ MXene. (a) Schematic illustration of the preparation process of Of-TiMX for eNO₃RR. (b-d) SEM, AFM and TEM images of TiMX. (e) TEM image of Of-TiMX. (f, i) HRTEM images of TiMX and Of-TiMX. The insets in (f) and (i) are the corresponding FFT images. (g, j) IFFT images of TiMX and Of-TiMX obtained by Fourier transform filtering. (h, k) Line analysis of TiMX and Of-TiMX. The zeros value on the axes in (h) and (k) correspond to the left end of the red lines in (g) and (j).

successful surface oxygen-functionalization of MXene, since Ti₃C₂O₂ has smaller lattice parameters compared to Ti₃C₂F₂ (Table S1).

The high resolution C 1s X-ray photoelectron spectroscopy (XPS) spectra for the samples showed peaks due to C-Ti, C=C/C-C, C=O/C-O and CF₂/CF₃ species (Fig. S5) [26,27]. A conspicuous change during the transformation of TiMX and Of-TiMX was the disappearance of the feature around 292 eV due to CF₂/CF₃ groups, providing strong evidence that the light oxidation treatment modified the functional groups on the MXene basal plane. The F 1s spectrum (Fig. 3a) of TiMX showed two intense peaks due to fluorine species (fluoride at low binding energy and CF₂/CF₃ groups at higher binding energy). The absence of fluorine signals in the F 1s spectrum of Of-TiMX indicated that the F-terminations and CF₂/CF₃ groups were totally removed or replaced by other terminations. Furthermore, the O 1s XPS spectrum of Of-TiMX (Fig. 3b) contained contributions from a number of oxygen species, with the Ti-O

signal being much stronger than was observed for TiMX, again suggesting that Of-TiMX contained more O-terminations [17].

Near-edge X-ray absorption fine structure (NEXAFS) provides very useful local coordination and bonding environment information [28]. The O K-edge spectra (Fig. 3c) for TiMX and Of-TiMX could be divided into two regions. The yellow shaded region on the left corresponds to the electron transfer from an occupied O 1s orbital into O 2p-Ti 3d hybrid orbitals, thus is very sensitive to the ligand coordination and local symmetry of the Ti cations. Two peaks are observed, corresponding to the t_{2g} and e_g states of octahedrally coordinated Ti cations. For Of-TiMX, the e_g feature at around 533.4 eV was almost as intense as the t_{2g} feature (whereas for TiMX the e_g feature was weak relative to the t_{2g} feature), implying a change in the surface composition. The lavender shaded area in Fig. 3c corresponds to excitations into higher energy levels involving covalent mixing of O 2p and Ti 4sp states and provides useful

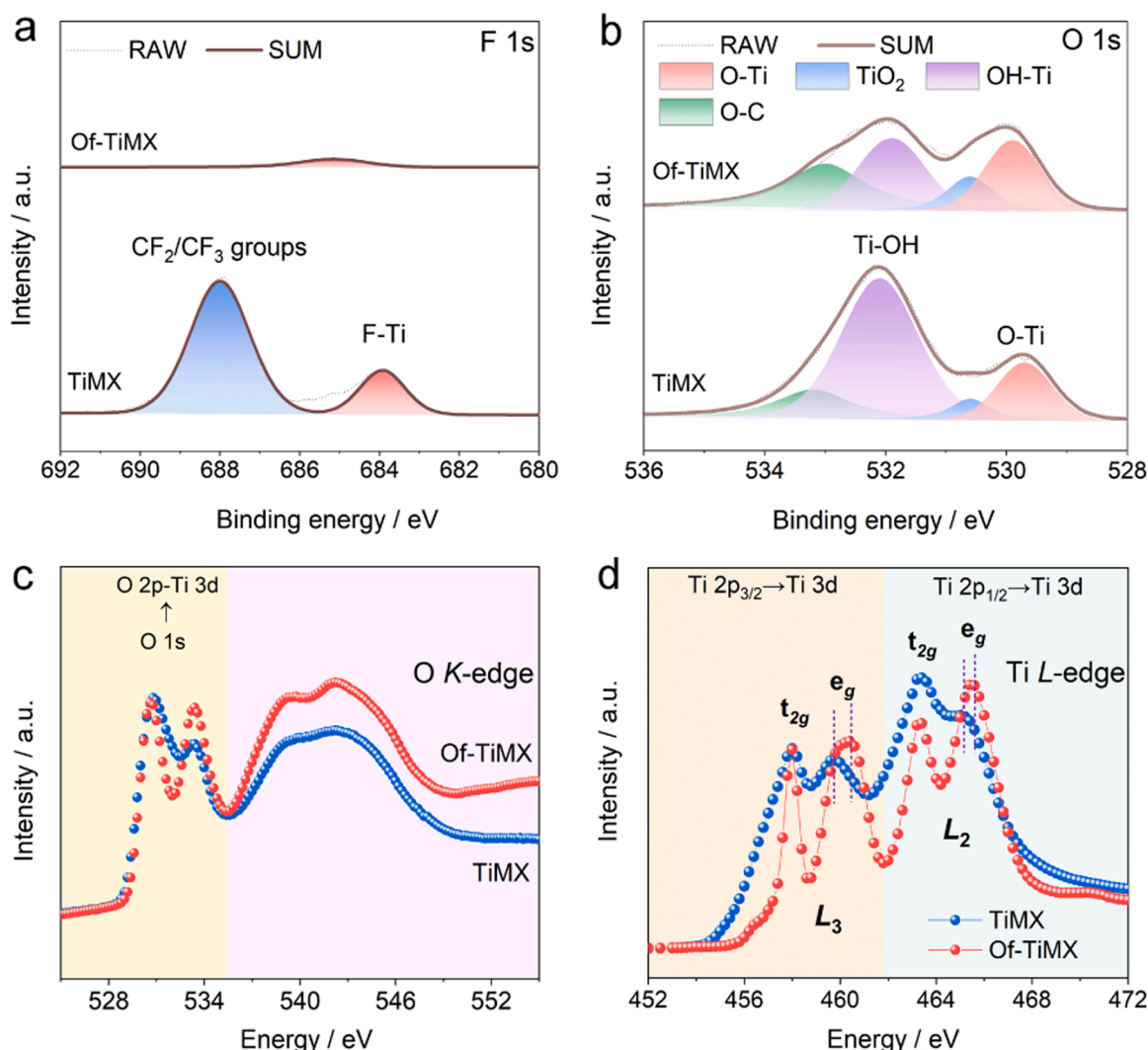


Fig. 3. Physical characterizations of the catalysts before and after oxygen functionalization. (a, b) XPS spectra for F 1s and O 1s of TiMX and Of-TiMX. (c, d) NEXAFS of O K-edge and Ti L-edge of TiMX and Of-TiMX.

“fingerprint” information about long-range order [28]. Since the spectra for both TiMX and Of-TiMX are similar in this region, it can be concluded that the intrinsic structure of the MXene was not changed by oxygen functionalization of the basal plane, consistent with the findings of the IFFT image analyses.

Ti $L_{2,3}$ -edge NEXAFS spectra for TiMX and Of-TiMX are shown in Fig. 3d. The Ti L_3 -edge signal involves Ti $2p_{3/2} \rightarrow Ti\ 3d$ transitions, whilst the Ti L_2 -edge signal involves Ti $2p_{1/2} \rightarrow Ti\ 3d$ transitions. Both signals are split into t_{2g} and e_g components, reflecting the distorted octahedral crystal field about the titanium cations in the samples. Comparing the Ti $L_{2,3}$ -edge NEXAFS spectra for TiMX and Of-TiMX, it is evident that the signals for TiMX occur at slightly lower photon energies. In addition, the onset of the absorption edges are also observed at lower photon energies for TiMX. Results are consistent with TiMX containing more Ti cations in low valence states (i.e. TiC, Ti^{2+} and Ti^{3+} sub-oxides) compared to Of-TiMX (with a higher proportion of Ti^{4+}). As with the XPS results (Fig. S6), the Ti $L_{2,3}$ -edge data indicates charge transfer from Ti to O atoms in Of-TiMX, offering compelling evidence for new Ti-O bonds being created through the surface oxygen-functionalization step [29].

3.2. Electrocatalytic nitrate reduction performance measurements

The eNO_3RR experiments were conducted in a H-type cell with a proton exchange membrane to separate the cathodic and anodic

compartments (Fig. 4a). A saturated calomel electrode (SCE) and a platinum foil (Pt-foil) were employed as the reference and counter electrodes, respectively. Linear sweep voltammetry (LSV) curves were collected to evaluate the eNO_3RR performance. The current density of the Of-TiMX working electrode (Fig. 4b) increased in the presence of NO_3^- , indicating that NO_3^- was involved in the reaction. After electrocatalysis at various potentials from $-1.5\ V$ to $-1.9\ V$ (vs. SCE), the concentration of nitrate (NO_3^-) and its reduction products (NO_2^- and NH_4^+) were quantified by ion chromatography (IC) (Figs. S7–S9). The total N-concentration including NO_3^- , NO_2^- and NH_4^+ did not change substantially as a function of the applied potential (Fig. S10). Further, no hydrazine (Fig. S11) or gaseous N_2 were detected as products. Thus, the extremely low NO_2^- concentration detected by IC demonstrated that the Of-TiMX electrocatalyst possessed excellent selectivity towards NH_3 . Based on the measured ion concentrations, Faradaic efficiencies (FEs) to NH_3 were calculated, which showed a volcano shape curve as a function of the applied potential during eNO_3RR (Fig. 4c). FEs in excess of 80 % were achieved over the potential range from -1.6 to $-1.9\ V$, with the ammonia formation rate of $0.99\ mg\ h^{-1}\ cm^{-2}$ and maximum FE of 90.4 % at an applied potential of $-1.7\ V$ (Figs. S12–S13). NH_3 has the largest partial current density over the examined potential range, with the hydrogen partial current density only becoming obvious at high applied potentials (Fig. 4d). Results indicate that Of-TiMX was very effective in suppressing HER during eNO_3RR . The nitrate reduction

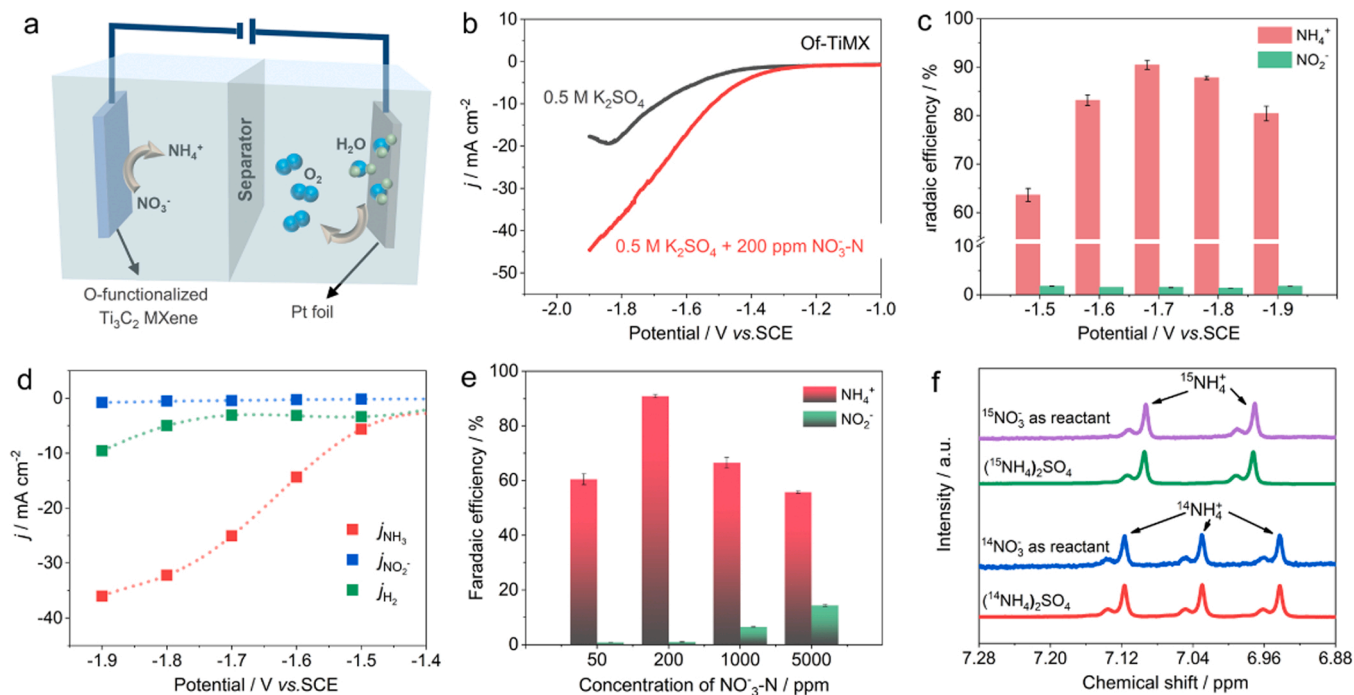


Fig. 4. Electrocatalytic nitrate reduction performance measurement. (a) Schematic illustration of electrocatalytic nitrate reduction. (b) LSV curves of Of-TiMX in 0.5 M K₂SO₄ and 0.5 M K₂SO₄ + 200 ppm NO₃-N electrolyte. (c) FEs of NH₄⁺ and NO₂⁻ for Of-TiMX at different potentials. (d) NH₃, NO₂ and H₂ partial current densities of Of-TiMX normalized by geometric area. (e) FEs of NH₄⁺ and NO₂⁻ for Of-TiMX at a potential of -1.7 V vs. SCE and different NO₃-N concentrations. (f) 600 MHz ¹H NMR spectra of the post-reaction electrolyte produced by using K¹⁵NO₃ and K¹⁴NO₃ as reactants. (¹⁵NH₄)₂SO₄ and (¹⁴NH₄)₂SO₄ are standard samples.

performance of TiMX and TiO₂ were also tested (Figs. S14–S15). The highest FE to NH₃ over TiMX was only 79.5 % (-1.6 V), which was significantly lower than that of Of-TiMX. Further, at this optimum potential gas bubbles were generated on the TiMX electrode, indicating that the lower FE was caused by the competitive HER.

Upon increasing the NO₃-N concentration, the current density of the

Of-TiMX working electrode showed a significant increase (Fig. S16), with the FEs to NH₃ at -1.7 V vs. SCE also showing a volcano shape curve trend (Fig. 4e). 200 ppm NO₃-N was the optimum concentration. At higher NO₃-N concentrations, there was increased production of NO₂, reducing the FE to NH₃. To verify that if the generated NH₃ on Of-TiMX come from the NO₃ reduction, control experiments were conducted

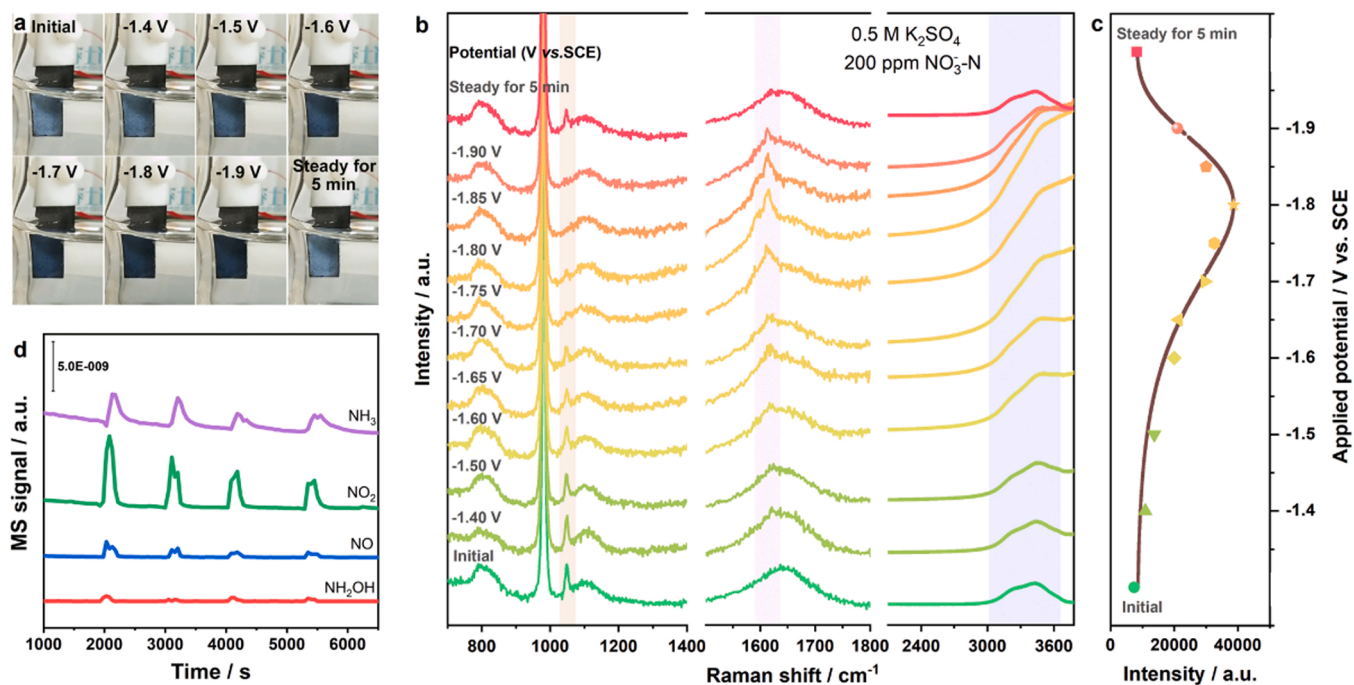


Fig. 5. Identification of surface states during reaction. (a) Photographs of the Of-TiMX electrode at different potentials. (b, c) In situ Raman spectra and hydroxyl peak intensity (light blue shaded area) of Of-TiMX for eNO₃RR under different applied potentials. (d) DEMS analysis of intermediates/products formed during eNO₃RR over Of-TiMX. Data for four consecutive cycles of eNO₃RR tests are shown.

using $^{15}\text{NO}_3$ (Fig. 4f). The 600 MHz ^1H nuclear magnetic resonance (NMR) spectra showed two peaks due to $^{15}\text{NH}_4^+$ at $\delta = 7.09$ and 6.97 ppm when K^{15}NO_3 was used as the reactant, whilst three peaks due to $^{14}\text{NH}_4^+$ were observed when K^{14}NO_3 was used as a reactant [30,31]. The isotope labeling experiments thus confirmed that the generated NH_3 originated from electrocatalytic NO_3^- reduction, eliminating the possibility of external environment contamination as a nitrogen source. By adding an external standard (maleic acid, $\text{C}_4\text{H}_4\text{O}_4$), the peak area of the ^1H NMR signal due to NH_4^+ showed a linear relationship with the concentration of NH_4^+ (Figs. S17–S18) [32]. The concentrations of $^{15}\text{NH}_4^+$ and $^{14}\text{NH}_4^+$ determined by ^1H NMR method were almost identical to those measured by IC (Fig. S19), indicating that the accuracy of the quantitative methods used in this work for NH_4^+ detection. Subsequently, the stability of Of-TiMX for eNO_3RR was investigated. The current density remains constant (Fig. S20) and the FEs of NH_3 remains around 90 % (Fig. S21) during the five consecutive recycling tests, indicating that the electrocatalyst possessed high catalytic stability.

3.3. Experimental mechanism studies

During the course of the eNO_3RR reaction, we found that the electrode surface of Of-TiMX would undergo a significant color change (Fig. 5a), turning from light blue to dark blue, with the original color being restored after 5 min of stabilization without an applied potential. The observed changes suggested that the electrocatalyst underwent reconstruction during the catalysis process [32]. To explore the realistic surface states, in situ Raman spectroscopy was applied to analyze the surface of Of-TiMX during the reaction (Fig. 5b) [33,34]. By increasing the applied potential, the band at 1049 cm^{-1} assigned to the ν_1 symmetric stretch of nitrate gradually disappeared [35]. The peak of 1615 cm^{-1} as the HOH bending mode of water revealed the hydrogen-bond interactions between interfacial water [36]. The broadened band at $3000\text{--}3600\text{ cm}^{-1}$ should be assigned to the O-H stretching band, which associated with coordinated hydrogen-bonded water [36]. The O-H band intensified with the applied potential up to -1.8 V (Fig. 5c), then decreased in intensity as higher potentials possibly due to the onset of HER. Results show that under the conditions of eNO_3RR , the basal layer of Of-TiMX is covered by terminal surface hydroxyl groups. Interestingly, changes in the abundance of surface hydroxyl groups correlated well with eNO_3RR activity, suggesting that interfacial H-bonding played a key role in nitrate/intermediate adsorption on the basal plane of Of-TiMX during eNO_3RR . In contrast, the in situ Raman spectra of TiMX showed little change under different applied potentials (Figs. S22–S23), indicating that Of-TiMX and TiMX were quite different in their surface properties and dynamic responsiveness to the applied potential.

The intermediates and products were detected by online differential electrochemical mass spectrometry (DEMS, Fig. 5d) [37,38]. At applied potentials from -1.0 to -1.9 V , three important reduction intermediates (NO_2 , NO , NH_2OH) and the final product NH_3 were detected by m/z signals at 46, 30, 33, and 17, respectively, over four continuous cycles. On the basis of the above analysis, surface functionalization of MXene by terminal oxygen is beneficial for promoting surface reconstruction during the electrocatalytic process, resulting in a hydroxyl-terminated surface that allows interfacial H-bonding with nitrate and other eNO_3RR intermediates. By this process, the inert basal plane of Ti_3C_2 MXene becomes active for nitrate reduction with suppressed HER activity, enhancing selectivity for eNO_3RR to NH_3 .

3.4. Density functional theory calculations

Density functional theory (DFT) calculations were used to explore the origin of the activity on Of-TiMX catalysts based on the reaction free energy diagrams. However, prior to analyzing the reaction mechanism of NH_3 synthesis, we first aimed to determine the surface state of the catalyst under the eNO_3RR experimental conditions, since a stable

surface state under electrochemical operating conditions plays a key role in determining the electrochemical reaction activities [39]. To this end, we established surface Pourbaix diagrams, to explore the thermodynamically most stable surface under particular reaction conditions, which could be then successfully used in rationalizing experimental eNO_3RR trends [40].

In determining phase transitions of interest, an O-terminated $\text{Ti}_3\text{C}_2\text{O}_2(001)$ surface with four surface oxygen atoms was selected as the initial calculation model for Of-TiMX (Figs. S24–S25). The calculated surface Pourbaix diagram as a function of potential (at $\text{pH} = 7$) is depicted in Fig. 6a, where a and b in the labels ($a\text{O} + b\text{OH}$) represent the number of O atoms and OH groups at the first layer (detail in Fig. S26). We found that at potentials starting at $\sim 0.0\text{ V}$ (vs. SCE), the $\text{Ti}_3\text{C}_2\text{O}_2(001)$ surface is fully covered by O^* , consistent with experimental data for Of-TiMX. On increasing the applied potential, the surface oxygen atoms are progressively protonated to form OH^* , with the surface covered with a combination of OH^* and O^* . The surface oxygen atoms were completely converted into hydroxyl on further increasing the applied potential, with oxygen vacancies forming via H_2O release at an even higher potential. This surface state evolution depicted in the surface Pourbaix diagram is in excellent agreement with the in situ experimental Raman test results for Of-TiMX (Fig. 5c), which showed inverted V-shaped trend of the amount of surface hydroxyl as the potential increased.

The surface Pourbaix diagram analysis and in-situ Raman studies established that Of-TiMX will have an OH-dominated basal surface under the experimental potentials used here for the eNO_3RR experiments (typically -1.7 V). We therefore studied the reaction mechanism for NH_3 synthesis on a fully OH-covered surface. We first investigated possible adsorption structures of nitrate and other intermediates formed during eNO_3RR , determining that all adsorbates bound with surface hydroxyl groups via H-bonding interactions. We used the step of $\text{NO}_2^* + (\text{H}^+ + \text{e}^-) \rightarrow \text{NOOH}^*$ here as an example to illustrate the role of surface hydroxyl and H-bonding in promoting eNO_3RR . As shown in Fig. 6b, the bond lengths between two O atoms in NO_2^* and adjacent surface hydroxyl protons were 1.63 and 1.69 \AA , respectively, implying the formation of H-bonding. The H atom in the hydroxyl was then transferred to NO_2^* to form NOOH^* , leaving an oxygen atom that rapidly interacted with H^* to form a new hydroxyl under the experimental potential, which then also participated in the formation of H-bonding between NOOH^* and the surface. This suggests that the H in a hydroxyl molecule will interact with the adsorbed species and participate in the subsequent hydrogenation process [20]. The surface hydroxyl groups were continuously replenished during the eNO_3RR . Since the surface hydroxyl groups facilitated adsorbate binding and served as a proton source for NH_3 production, they could be viewed as both an active site and reactant, respectively [41]. Further, since the H preferentially adsorbed on surface O atoms in nitrate reduction, the formation of H_2 was largely suppressed. A detailed comparison of activity between HER and eNO_3RR was performed and showed in Fig. S27. These theoretical analyses were consistent with our experimental observations, with the activity of HER being negligible relative to NH_3 synthesis at potentials of -1.7 V and below.

A free energy diagram for eNO_3RR on the fully OH-covered Of-TiMX surface was then created based on the calculated adsorption free energies of nitrate and other intermediates. We investigated several possible reaction pathways for NH_3 synthesis via eNO_3RR on the fully OH-covered Of-TiMX surface, and identified the most favorable pathway (Fig. 6c and Table S2), involving the following steps: $\text{NO}_3^- \xrightarrow{\text{H}^+} \text{HNO}_3^* \xrightarrow{\text{H}^+ + \text{e}^-} \text{NO}_2^* \xrightarrow{\text{H}^+ + \text{e}^-} \text{NOOH}^* \xrightarrow{\text{H}^+ + \text{e}^-} \text{NO}^* \xrightarrow{\text{H}^+ + \text{e}^-} \text{NHO}^* \xrightarrow{\text{H}^+ + \text{e}^-} \text{NH}_2\text{O}^* \xrightarrow{\text{H}^+ + \text{e}^-} \text{NH}_2\text{OH}^* \xrightarrow{\text{H}^+ + \text{e}^-} \text{NH}_2^* \xrightarrow{\text{H}^+ + \text{e}^-} \text{NH}_3^*$. Significantly, two key adsorbates, NO^* and NH_2OH^* , were also detected experimentally by DEMS (Fig. 5d), which corroborates our calculated reaction mechanism.

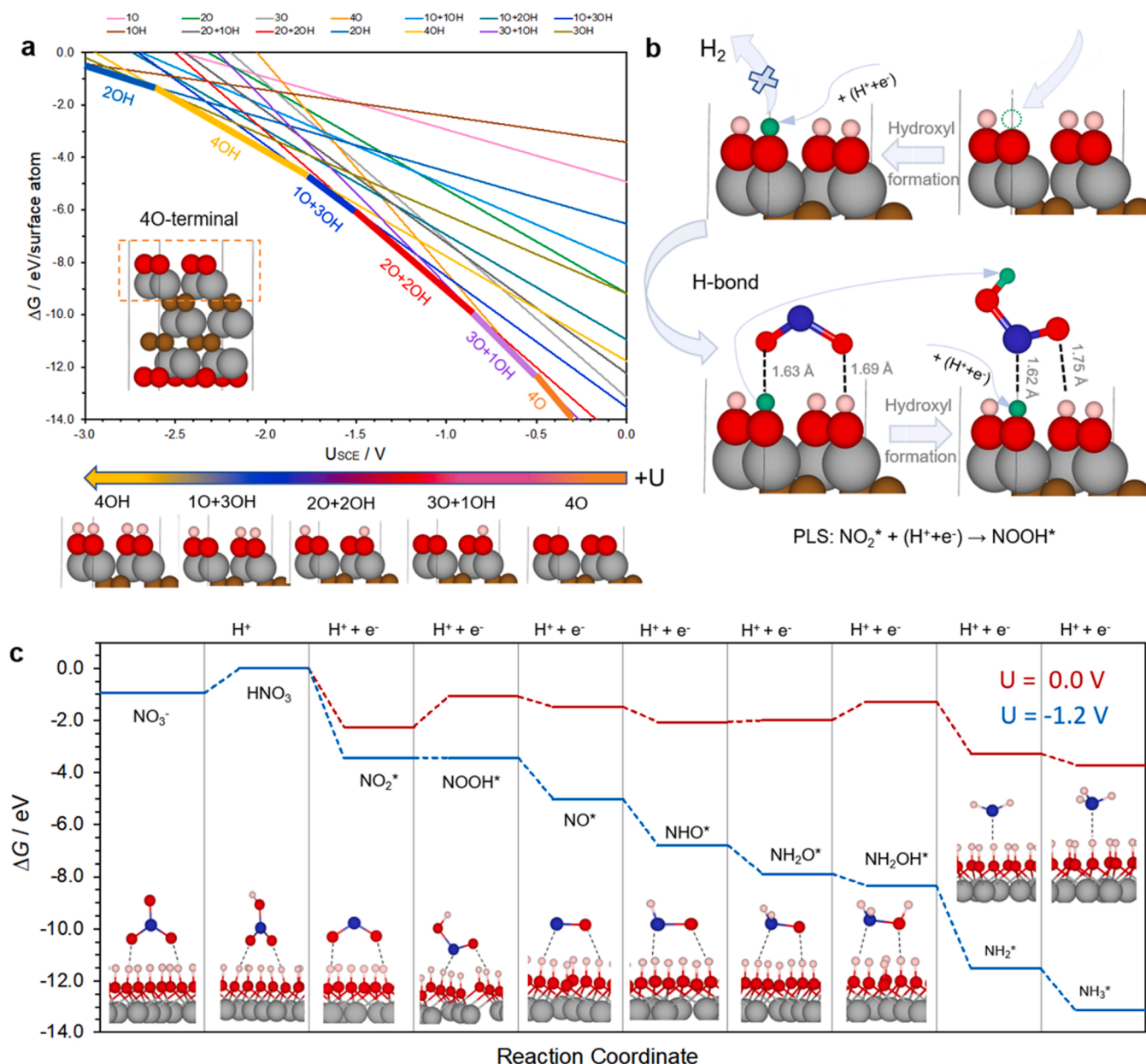


Fig. 6. DFT calculations of the eNO₃RR reaction mechanism and adsorbate structures. (a) Calculated surface Pourbaix diagrams for Of-TiMX as a function of potential at pH = 7. Grey, brown, red, and pink spheres represent Ti, C, O, and H atoms, respectively. (b) Illustration of the surface hydroxyl and H-bond formation in the potential-limiting step involving the reduction of NO_2^* to NOOH^* . Grey, brown, red, pink/green, and blue spheres represent Ti, C, O, H, and N atoms, respectively. Dashed black lines represent the H-bonding interactions. (c) Free-energy diagrams for NO_3^- reduction to NH_3 on the surface of full OH-terminated Of-TiMX at $U = 0.0$ V (red line) and $U = -1.2$ V vs. SHE (blue line). Insets are the optimized configurations for adsorbates, where the dashed black lines represent the H-bonding interactions.

Additionally, N_2 was not detected as a product in our eNO₃RR experiments using the Of-TiMX catalyst, which agrees well with our DFT calculations. The calculated potential-limiting step is the reduction of NO_2^* to NOOH^* , with a limiting potential of -1.2 V vs. RHE. In comparison to previously reported highly active metal catalysts for eNO₃RR [42–45], the limiting potential over the Of-TiMX model catalyst is larger, implying slightly lower activity compared to state-of-the-art metal catalysts. This is not surprising, since the adsorption sites on Of-TiMX are surface hydroxyl groups, rather than metal sites which bind adsorbates more strongly through covalent bonding. If one can find a way to achieve some highly active metal Ti states on MXene-based catalysts, the activity will be significantly enhanced. Therefore, both experimentally and theoretically, we have demonstrated here a new active site (surface hydroxyl) and a novel reaction mechanism for

eNO₃RR involving H-bonding between adsorbates and the catalyst surface, which adequately explains the high applied potentials and low selectivity for HER on the full OH-terminated Ti₃C₂ MXene.

4. Conclusions

In summary, the electrocatalytic reduction of nitrate to ammonia on Of-TiMX was performed both experimentally and theoretically. It revealed that the surface hydroxyl on Of-TiMX plays a key role on the eNO₃RR process. This work is expected to attract significant interest from the catalysis community for a number of reasons. Firstly, the exploration of a realistic surface state, especially the active sites, is extremely important before further theoretical activity analysis. Secondly, we identified that surface hydroxyl played a key role as the reaction medium in the

reductive-hydrogenolysis of nitrate to NH_3 , by inhibiting H_2 formation. In addition, the potential-limiting step of NH_3 synthesis on the Of-TiMX surface was the reduction of NO_2^* to NOOH^* . By additional surface modifications (such as doping Of-TiMX), it should be possible to enhance the adsorption of NOOH^* , thereby delivering very active NH_3 synthesis catalysts. Finally, we have reported for the first time a novel hydrogen bonding-mediated reaction mechanism for NH_3 synthesis on OH-dominated Of-TiMX surfaces, opening new vistas toward high performance catalysts for eNO_3RR and other PCET-related reactions.

CRedit authorship contribution statement

Conceptualization, J.C., S.L., and S.Q.Z.; Methodology, J.C., J.H., and A.C.; Investigation, J.C., J.H., Y.W., H.W., J.L., J.Y., X.L., and Z.J.; Writing – original draft, J.C. and A.C.; Writing – review & editing, G.I. N.W. and S.L.; Funding acquisition, J.C., S.L., and S.Q.Z.; Supervision, S.Q.Z.

Declaration of Competing Interest

The authors declare that they have no known competing financial interests or personal relationships that could have appeared to influence the work reported in this paper.

Data Availability

Data will be made available on request.

Acknowledgements

Jinmeng Cai, and Jingjing Huang contributed equally to this work. This work was supported by the National Natural Science Foundation of China (No. 22205213), the China Postdoctoral Science Foundation (2020M682332, 2021T140614), the National Science Foundation of Henan Province (222300420287), and Henan Postdoctoral Foundation (202003015). GINW is supported by a James Cook Research Fellowship, administered by the Royal Society Te Apārangi.

Appendix A. Supporting information

Supplementary data associated with this article can be found in the online version at [doi:10.1016/j.apcatb.2023.122473](https://doi.org/10.1016/j.apcatb.2023.122473).

References

- [1] Y. Wu, Z. Jiang, Z. Lin, Y. Liang, H. Wang, Direct electrosynthesis of methylamine from carbon dioxide and nitrate, *Nat. Sustain.* 4 (2021) 725–730.
- [2] Y. Li, C. Cheng, S. Han, Y. Huang, X. Du, B. Zhang, Y. Yu, Electrocatalytic reduction of low-concentration nitric oxide into ammonia over Ru nanosheets, *ACS Energy Lett.* 7 (2022) 1187–1194.
- [3] Y. Wang, Y. Yu, R. Jia, C. Zhang, B. Zhang, Electrochemical synthesis of nitric acid from air and ammonia through waste utilization, *Natl. Sci. Rev.* 6 (2019) 730–738.
- [4] J. Guo, M. Wang, L. Xu, X. Li, A. Iqbal, G.E. Sterbinsky, H. Yang, M. Xie, J. Zai, Z. Feng, T. Cheng, X. Qian, Bioinspired activation of N_2 on asymmetrical coordinated Fe grafted 1T MoS_2 at room temperature, *Chin. J. Chem.* 39 (2021) 1898–1904.
- [5] J. Wang, T. Feng, J. Chen, V. Ramalingam, Z. Li, D.M. Kabtamu, J.-H. He, X. Fang, Electrocatalytic nitrate/nitrite reduction to ammonia synthesis using metal nanocatalysts and bio-inspired metalloenzymes, *Nano Energy* 86 (2021), 106088.
- [6] J. Cai, Y. Wei, A. Cao, J. Huang, Z. Jiang, S. Lu, S.-Q. Zang, Electrocatalytic nitrate-to-ammonia conversion with ~100 % Faradaic efficiency via single-atom alloying, *Appl. Catal. B-Environ.* 316 (2022), 121683.
- [7] J. Li, G. Zhan, J. Yang, F. Quan, C. Mao, Y. Liu, B. Wang, F. Lei, L. Li, A.W.M. Chan, L. Xu, Y. Shi, Y. Du, W. Hao, P.K. Wong, J. Wang, S.-X. Dou, L. Zhang, J.C. Yu, Efficient ammonia electrosynthesis from nitrate on strained ruthenium nanoclusters, *J. Am. Chem. Soc.* 142 (2020) 7036–7046.
- [8] G.-F. Chen, Y. Yuan, H. Jiang, S.-Y. Ren, L.-X. Ding, L. Ma, T. Wu, J. Lu, H. Wang, Electrochemical reduction of nitrate to ammonia via direct eight-electron transfer using a copper-molecular solid catalyst, *Nat. Energy* 5 (2020) 605–613.
- [9] Y. Li, H. Shao, Z. Lin, J. Lu, L. Liu, B. Duployer, P.O.Å. Persson, P. Eklund, L. Hultman, M. Li, K. Chen, X.-H. Zha, S. Du, P. Rozier, Z. Chai, E. Raymundo-Piñero, P.-L. Taberna, P. Simon, Q. Huang, A general Lewis acidic etching route for preparing MXenes with enhanced electrochemical performance in non-aqueous electrolyte, *Nat. Mater.* 19 (2020) 894–899.
- [10] G. Gao, A.P. O'Mullane, A. Du, 2D MXenes: a new family of promising catalysts for the hydrogen evolution reaction, *ACS Catal.* 7 (2017) 494–500.
- [11] J. Peng, X. Chen, W.-J. Ong, X. Zhao, N. Li, Surface and heterointerface engineering of 2D MXenes and their nanocomposites: insights into electro- and photocatalysis, *Chem* 5 (2019) 18–50.
- [12] Y. Gao, Y. Cao, H. Zhuo, X. Sun, Y. Gu, G. Zhuang, S. Deng, X. Zhong, Z. Wei, X. Li, J.-G. Wang, Mo_2TiC_2 MXene: a promising catalyst for electrocatalytic ammonia synthesis, *Catal. Today* 339 (2020) 120–126.
- [13] L. Li, X. Wang, H. Guo, G. Yao, H. Yu, Z. Tian, B. Li, L. Chen, Theoretical screening of single transition metal atoms embedded in MXene defects as superior electrocatalyst of nitrogen reduction reaction, *Small Methods* 3 (2019), 1900337.
- [14] Y. Luo, G.-F. Chen, L. Ding, X. Chen, L.-X. Ding, H. Wang, Efficient electrocatalytic N_2 fixation with MXene under ambient conditions, *Joule* 3 (2019) 279–289.
- [15] Y. Guo, T. Wang, Q. Yang, X. Li, H. Li, Y. Wang, T. Jiao, Z. Huang, B. Dong, W. Zhang, J. Fan, C. Zhi, Highly efficient electrochemical reduction of nitrogen to ammonia on surface termination modified $\text{Ti}_3\text{C}_2\text{T}_x$ MXene nanosheets, *ACS Nano* 14 (2020) 9089–9097.
- [16] C. Ling, L. Shi, Y. Ouyang, J. Wang, Searching for highly active catalysts for hydrogen evolution reaction based on O-terminated MXenes through a simple descriptor, *Chem. Mater.* 28 (2016) 9026–9032.
- [17] X. Chen, Y. Zhu, M. Zhang, J. Sui, W. Peng, Y. Li, G. Zhang, F. Zhang, X. Fan, N-butyl lithium-treated $\text{Ti}_3\text{C}_2\text{T}_x$ MXene with excellent pseudocapacitor performance, *ACS Nano* 13 (2019) 9449–9456.
- [18] A.D. Handoko, K.H. Khoo, T.L. Tan, H. Jin, Z.W. Seh, Establishing new scaling relations on two-dimensional MXenes for CO_2 electroreduction, *J. Mater. Chem. A* 6 (2018) 21885–21890.
- [19] V. Parey, B.M. Abraham, M.V. Jyothirmai, J.K. Singh, Mechanistic insights for electrochemical reduction of CO_2 into hydrocarbon fuels over O-terminated MXenes, *Catal. Sci. Technol.* 12 (2022) 2223–2231.
- [20] T. Wang, Y. Zhang, B. Huang, B. Cai, R.R. Rao, L. Giordano, S.-G. Sun, Y. Shao-Horn, Enhancing oxygen reduction electrocatalysis by tuning interfacial hydrogen bonds, *Nat. Catal.* 4 (2021) 753–762.
- [21] Z. Gao, J. Mu, J. Zhang, Z. Huang, X. Lin, N. Luo, F. Wang, Hydrogen bonding promotes alcohol C-C coupling, *J. Am. Chem. Soc.* 144 (2022) 18986–18994.
- [22] M. Naguib, M. Kurtoglu, V. Presser, J. Lu, J. Niu, M. Heon, L. Hultman, Y. Gogotsi, M.W. Barsoum, Two-dimensional nanocrystals produced by exfoliation of Ti_3AlC_2 , *Adv. Mater.* 23 (2011) 4248–4253.
- [23] L.-X. Li, W.-J. Sun, H.-Y. Zhang, J.-L. Wei, S.-X. Wang, J.-H. He, N.-J. Li, Q.-F. Xu, D.-Y. Chen, H. Li, J.-M. Lu, Highly efficient and selective nitrate electroreduction to ammonia catalyzed by molecular copper catalyst@ $\text{Ti}_3\text{C}_2\text{T}_x$ MXene, *J. Mater. Chem. A* 9 (2021) 21771–21778.
- [24] M. Shen, W. Jiang, K. Liang, S. Zhao, R. Tang, L. Zhang, J.Q. Wang, One-pot green process to synthesize MXene with controllable surface terminations using molten salts, *Angew. Chem. Int. Ed.* 60 (2021) 27013–27018.
- [25] I. Persson, J. Halim, T.W. Hansen, J.B. Wagner, V. Darakchieva, J. Palisaitis, J. Rosen, P.O. Persson, How much oxygen can a MXene surface take before it breaks? *Adv. Funct. Mater.* 30 (2020), 1909005.
- [26] L. Zhao, B. Dong, S. Li, L. Zhou, L. Lai, Z. Wang, S. Zhao, M. Han, K. Gao, M. Lu, X. Xie, B. Chen, Z. Liu, X. Wang, H. Zhang, H. Li, J. Liu, H. Zhang, X. Huang, W. Huang, Interdiffusion reaction-assisted hybridization of two-dimensional metal-organic frameworks and $\text{Ti}_3\text{C}_2\text{T}_x$ nanosheets for electrocatalytic oxygen evolution, *ACS Nano* 11 (2017) 5800–5807.
- [27] V. Ramalingam, P. Varadhan, H.-C. Fu, H. Kim, D. Zhang, S. Chen, L. Song, D. Ma, Y. Wang, H.N. Alshareef, J.-H. He, Heteroatom-mediated interactions between ruthenium single atoms and an MXene support for efficient hydrogen evolution, *Adv. Mater.* 31 (2019), 1903841.
- [28] V.S. Lusvardi, M.A. Barteau, J.G. Chen, J. Eng Jr, B. Fröhberger, A. Teplyakov, An NEXAFS investigation of the reduction and reoxidation of $\text{TiO}_2(001)$, *Surf. Sci.* 397 (1998) 237–250.
- [29] A. Braun, K.K. Akurati, G. Fortunato, F.A. Reifler, A. Ritter, A.S. Harvey, A. Vital, T. Graule, Nitrogen doping of TiO_2 photocatalyst forms a second e_g state in the oxygen 1s NEXAFS pre-edge, *J. Phys. Chem. C* 114 (2009) 516–519.
- [30] R. Jia, Y. Wang, C. Wang, Y. Ling, Y. Yu, B. Zhang, Boosting selective nitrate electroreduction to ammonium by constructing oxygen vacancies in TiO_2 , *ACS Catal.* 10 (2020) 3533–3540.
- [31] W.J. Sun, H.Q. Ji, L.X. Li, H.Y. Zhang, Z.K. Wang, J.H. He, J.M. Lu, Built-in electric field triggered interfacial accumulation effect for efficient nitrate removal at ultra-low concentration and electroreduction to ammonia, *Angew. Chem. Int. Ed.* 60 (2021) 22933–22939.
- [32] Y. Wang, W. Zhou, R. Jia, Y. Yu, B. Zhang, Unveiling the activity origin of a copper-based electrocatalyst for selective nitrate reduction to ammonia, *Angew. Chem. Int. Ed.* 59 (2020) 5350–5354.
- [33] R. Daiyan, T. Tran-Phu, P. Kumar, K. Iputera, Z.Z. Tong, J. Leverett, M.H.A. Khan, A.A. Esmailpour, A. Jalili, M. Lim, A. Tricoli, R.S. Liu, X.Y. Lu, E. Lovell, R. Amal, Nitrate reduction to ammonium: from CuO defect engineering to waste NO_x -to- NH_3 economic feasibility, *Energy Environ. Sci.* 14 (2021) 3588–3598.
- [34] X. Lu, J. Yu, J. Cai, Q. Zhang, S. Yang, L. Gu, G.I.N. Waterhouse, S.-Q. Zang, B. Yang, S. Lu, Exclusive nitrate to ammonia conversion via boron-doped carbon dots induced surface Lewis acid sites, *Cell Rep. Phys. Sci.* 3 (2022), 100961.
- [35] W. He, J. Zhang, S. Dieckhöfer, S. Varhade, A.C. Brix, A. Lielpetere, S. Seisel, J.R. C. Junqueira, W. Schuhmann, Splicing the active phases of copper/cobalt-based catalysts achieves high-rate tandem electroreduction of nitrate to ammonia, *Nat. Commun.* 13 (2022) 1129.

- [36] Y.-H. Wang, S. Zheng, W.-M. Yang, R.-Y. Zhou, Q.-F. He, P. Radjenovic, J.-C. Dong, S. Li, J. Zheng, Z.-L. Yang, G. Attard, F. Pan, Z.-Q. Tian, J.-F. Li, In situ Raman spectroscopy reveals the structure and dissociation of interfacial water, *Nature* 600 (2021) 81–85.
- [37] W.-J. Sun, L.-X. Li, H.-Y. Zhang, J.-H. He, J.-M. Lu, A bioinspired iron-centered electrocatalyst for selective catalytic reduction of nitrate to ammonia, *ACS Sustain. Chem. Eng.* 10 (2022) 5958–5965.
- [38] J. Wang, T. Feng, J. Chen, J.H. He, X. Fang, Flexible 2D Cu metal: organic framework@MXene film electrode with excellent durability for highly selective electrocatalytic NH_3 synthesis, *Research* 2022 (2022), 9837012.
- [39] O. Vinogradova, D. Krishnamurthy, V. Pande, V. Viswanathan, Quantifying confidence in DFT-predicted surface pourbaix diagrams of transition-metal electrode–electrolyte interfaces, *Langmuir* 34 (2018) 12259–12269.
- [40] H. Li, S. Kelly, D. Guevarra, Z. Wang, Y. Wang, J.A. Haber, M. Anand, G.T.K. K. Gunasooriya, C.S. Abraham, S. Vijay, J.M. Gregoire, J.K. Nørskov, Analysis of the limitations in the oxygen reduction activity of transition metal oxide surfaces, *Nat. Catal.* 4 (2021) 463–468.
- [41] D.S. Potts, D.T. Bregante, J.S. Adams, C. Torres, D.W. Flaherty, Influence of solvent structure and hydrogen bonding on catalysis at solid–liquid interfaces, *Chem. Soc. Rev.* 50 (2021) 12308–12337.
- [42] Z.-Y. Wu, M. Karamad, X. Yong, Q. Huang, D.A. Cullen, P. Zhu, C. Xia, Q. Xiao, M. Shakouri, F.-Y. Chen, J.Y. Kim, Y. Xia, K. Heck, Y. Hu, M.S. Wong, Q. Li, I. Gates, S. Siahrostami, H. Wang, Electrochemical ammonia synthesis via nitrate reduction on Fe single atom catalyst, *Nat. Commun.* 12 (2021) 2870.
- [43] Y. Wang, A. Xu, Z. Wang, L. Huang, J. Li, F. Li, J. Wicks, M. Luo, D.-H. Nam, C.-S. Tan, Y. Ding, J. Wu, Y. Lum, C.-T. Dinh, D. Sinton, G. Zheng, E.H. Sargent, Enhanced nitrate-to-ammonia activity on copper–nickel alloys via tuning of intermediate adsorption, *J. Am. Chem. Soc.* 142 (2020) 5702–5708.
- [44] Y. Zhang, X. Chen, W. Wang, L. Yin, J.C. Crittenden, Electrocatalytic nitrate reduction to ammonia on defective Au_1Cu (111) single-atom alloys, *Appl. Catal. B-Environ.* 310 (2022), 121346.
- [45] Y.M. Wang, J. Cai, Q.Y. Wang, Y. Li, Z. Han, S. Li, C.H. Gong, S. Wang, S.Q. Zang, T.C.W. Mak, Electropolymerization of metal clusters establishing a versatile platform for enhanced catalysis performance, *Angew. Chem. Int. Ed.* 61 (2022), e202114538.